JOURNAL OF VIROLOGY, Aug. 2011, p. 7797–7809 Vol. 85, No. 15
0022-538X/11/$12.00 doi:10.1128/JVI.02465-10

Contribution of Topology Determinants of a Viral Movement Protein to Its Membrane Association, Intracellular Traffic, and Viral Cell-to-Cell Movement▽†

A. Genovés,‡ V. Pallás,* and J. A. Navarro

Instituto de Biología Molecular y Celular de Plantas, IBMCP (Universitat Politècnica de València-Consejo Superior de Investigaciones Científicas) Avenida Ingeniero Fausto Elio, s/n 46022, Valencia, Spain

Received 25 November 2010/Accepted 6 May 2011

The p7B movement protein (MP) of *Melon necrotic spot virus* (MNSV) is a single-pass membrane protein associated with the endoplasmic reticulum (ER), the Golgi apparatus (GA), and plasmodesmata (Pd). Experimental data presented here revealed that the p7B transmembrane domain (TMD) was sufficient to target the green fluorescent protein (GFP) to ER membranes. In addition, the short extramembrane regions of p7B were essential for subsequent ER export and transport to the GA and Pd. Microsomal partitioning and bimolecular fluorescence assays supported a type II topology of p7B *in planta*. Mutations affecting conventional determinants of p7B membrane topology, such as the TMD secondary structure, the overall hydrophobicity profile, the so-called "aromatic belt," and the net charge distribution on either side of the TMD, were engineered into infectious RNAs to investigate the relationship between the MP structure and MNSV cell-to-cell movement. The results revealed that (i) the overall hydrophobic profile and the α-helix integrity of the TMD were relevant for virus movement, (ii) modification of the net charge balance of the regions flanking both TMD sides drastically reduced cell-to-cell movement, (iii) localization of p7B to the GA was necessary but not sufficient for virus movement, and (iv) membrane insertion was essential for p7B function in virus movement. Our results therefore indicate that MNSV cell-to-cell movement requires sequential transport of p7B from the ER via the GA to Pd, which is modulated by a combination of several signals with different strengths in the extramembrane regions and TMD of the MP.

The association of plant positive-strand RNA viruses with plant cell endomembranes is a critical event that occurs during the virus life cycle. Many viral factors are proteins containing hydrophobic regions that generally induce drastic modifications in endoplasmic reticulum (ER) morphology, the nuclear envelope, and other membrane-bound organelles. These cytopathic rearrangements result in the formation of membrane-associated invaginations, free cytoplasmic vesicles, or multivesicular bodies that provide protective environments and enlarged surfaces, not only for genome replication, translation, and particle assembly, but also for intracellular and cell-to-cell movement (1, 33, 39, 53).

How plant viruses take advantage of the intracellular endomembrane system to move appears to be related to the structural characteristics of one or more virus-encoded movement proteins (MPs) (37, 52, 55). For example, *Tobacco mosaic virus* (TMV) MP is a tightly associated membrane protein that was proposed to contain two helical hydrophobic domains spanning the ER membrane (8, 16). TMV MP, together with the TMV 126-kDa protein, which, respectively, have movement and replication functions, cause a transient aggregation of the ER, resulting in the formation of cytoplasmic membrane bodies where TMV replicates (viral replication complexes [VRCs]) (23, 31). These viral factories travel toward the cell host periphery in a cytoskeleton-dependent manner, resulting in entry into neighboring cells by traversing the cell wall through the plasmodesmata (Pd) (24, 49). MP association with ER membranes has also been described for viruses whose MPs induce tubule formation in Pd. For example, *Alfalfa mosaic virus* (AMV) MP behaves as an integral membrane protein and localizes to the ER (30). In addition, *Prunus necrotic ringspot virus* (PNRSV) MP has one hydrophobic region that mediates its association with biological membranes. However, this region is not thought to traverse the entire lipid bilayer but rather is embedded in the membrane interface with the N and C termini oriented toward the cytoplasm (41). The intracellular transport and cell-to-cell movement of some flexible rod viruses belonging to nine different genera are driven by the triple-gene block of movement proteins (TGBp1, TGBp2, and TGBp3). TGBp1s are multifunctional RNA-binding proteins. All TGBp2s contain two transmembrane domains (TMDs), whereas TGBp3s form two main groups having either one (the potex-like group) or two (the hordei-like group) TMDs. Several groups have reported that the interactions among the three components of the TGB module might differ depending on virus genera, with four models recently proposed to summarize the collective findings (57). Regardless of the interaction model and virus, TGB2 and TGB3 proteins are always associated with ER membranes and, occasionally, with ER-derived vesicles, which move along the actin network to reach the Pd (57).

* Corresponding author. Mailing address: Instituto de Biología Molecular y Celular de Plantas (IBMCP), UPV-CSIC, Avenida Ingeniero Fausto Elio, s/n, 46022, Valencia, Spain. Phone: 34 963877877. Fax: 34 963877859. E-mail: vpallas@ibmcp.upv.es.

‡ Present address: Centro de Investigación Príncipe Felipe, Avenida Autopista del Saler, 16, E-46013, Valencia, Spain.

† Supplemental material for this article may be found at http://jvi.asm.org/.

▽ Published ahead of print on 18 May 2011.

Association of viral MPs with plant endomembranes has also been reported for p6 of *Beet yellows virus* (BYV) and for p7B of *Melon necrotic spot virus* (MNSV) (20, 44). Both proteins contain a very hydrophobic TMD that inserts into the ER membrane. Interestingly, the most important difference between these MPs is that p7B moves from the ER to the Golgi apparatus (GA), followed by targeting to Pd (20), while BYV p6 remains in the ER membrane (44). The ER-GA-Pd pathway described for p7B migration has also been observed for cellular proteins, such as the class 1 reversibly glycosylated polypeptides and the family of plasmodesmata-located proteins (PDLP1) (48, 56).

The MNSV p7B is one of the two small MPs encoded by carmoviruses that are essential for virus cell-to-cell movement (18). By using *in vitro* translation assays in the presence of canine pancreas rough microsomes, it was recently demonstrated that membrane association of p7B requires its TMD (42). Moreover, as occurs for most integral membrane proteins, the p7B TMD adopts an α-helix conformation that is cotranslationally inserted into the lipidic bilayer through the ER translocon (40). The translocation machineries play a central role in helix bundle membrane protein topology, controlling TMD insertion and orientation into lipid bilayers (25). The total hydrophobicity and helix arrangement of the TMD, together with the distribution of aromatic and charged amino acids on either side of the hydrophobic region, are critical features that affect TMD-lipid bilayer interaction and, consequently, TMD recognition in the ribosome-translocon channel (27, 34, 59, 60).

While viral MPs have been shown to interact with biological membranes, our knowledge about the role of MP membrane topology in MP transport to Pd and in viral cell-to-cell movement has been largely restricted to TMV-like MPs and the TGB system (29, 57). Therefore, extending these studies to other viruses with different types of MPs should allow a better understanding of virus-plant interactions. For this report, we investigated whether membrane association, intracellular transport of p7B, and MNSV cell-to-cell movement were influenced by altering topological determinants of the MP.

MATERIALS AND METHODS

Construction of binary vectors for p7B membrane topology studies and site-directed mutagenesis. The MNSV p7B open reading frame (ORF) was PCR amplified from plasmid pMNSV(Al) (accession number DQ339157) (18). Amino-terminal (N_t) and carboxy-terminal (C_t) fusions of MNSV p7B to the N-terminal fragment (residues 1 to 155) of the yellow fluorescent protein (YFP) (p7B-N_t[YFP] and N_t[YFP]-p7B, respectively) were cloned into the binary vector pMOG 800 between the *Cauliflower mosaic virus* (CaMV) 35S promoter and the potato proteinase inhibitor II terminator (PoPit) (32). CaMV 35S expression cassettes corresponding either to the ER-targeted N_t[YFP] (ER-N_t[YFP]) or to the ER-targeted C-terminal fragment (residues 156 to 238) of the YFP (ER-C_t[YFP]) were obtained by HindIII digestion of pRT-YN-ER and pRT-YC-ER, respectively (62), and then cloned into HindIII-linearized pMOG800. The pRT-YN-ER and pRT-YC-ER plasmids were kindly provided by J. P. T. Valkonen. Binary vectors expressing either the N_t[YFP] or C_t[YFP] cytosolic fragment were previously described (3).

Site-directed mutations were introduced into the p7B ORF of the pMNSV(Al)-Δcp-GFP clone, from which infectious RNAs expressing the green fluorescent protein (GFP) can be obtained (18, 19). For subcellular localization in *Nicotiana benthamiana*, mutations were incorporated into the previously described binary vector expressing GFP-p7B (20). For membrane orientation studies in *N. benthamiana*, several mutations were introduced into binary vectors expressing either p7B-N_t[YFP] or N_t[YFP]-p7B. The QuickChangeR XL-Site-Directed Mutagenesis Kit (Stratagene, La Jolla, CA) and the primer pairs enumerated in Table S1 in the supplemental material were used.

***In vitro* transcription and plant inoculation.** Viral cell-to-cell movement was assayed as previously described (18, 19). Briefly, infectious RNAs were obtained from pMNSV(Al)-Δcp-GFP clones containing either the wild-type p7B or each mutant variant ORF (see Table S1 in the supplemental material). Transcripts were inoculated in *Cucumis melo* (cv. Galia) cotyledons transiently expressing MNSV coat protein (p42) (18, 19). At least, three independent bioassays with five plants per mutant RNA were performed. At 3 days postinoculation (p.i.), 20 to 30 images of individual fluorescent infection foci were taken with a confocal microscope (Leica TCS SL; Leica Microsystems GmbH, Wetzlar, Germany). Fluorescent infection areas were measured using ImageJ 1.41o software, and data were analyzed with Microsoft Excel.

***Agrobacterium tumefaciens*-mediated transient-expression and bimolecular fluorescence complementation assays.** Transient-expression assays on *N. benthamiana* plants were performed as previously described (18). Briefly, the binary constructs were introduced into *Agrobacterium tumefaciens* strain C58C1 by electroporation (GenePulser Xcell electroporation system; Bio-Rad Laboratories, Hercules, CA). Transformed bacteria were grown overnight in a shaking incubator at 28°C in Luria-Bertani (LB) medium supplemented with the appropriate antibiotic mixture. The cultures were collected by low-speed centrifugation and adjusted to the required final optical density at 600 nm (OD_{600}) value (0.2) with 10 mM $MgCl_2$, 10 mM morpholineethanesulfonic acid (MES), pH 5.6, and 150 μM acetosyringone. These suspensions were infiltrated into 2-week-old *N. benthamiana* plants by gentle pressure infiltration into the lower side of the leaves. For colocalization and bimolecular fluorescence complementation (BiFC) experiments requiring the simultaneous expression of two or more different proteins, individual bacterial cultures containing the corresponding binary vectors were adjusted to a final OD_{600} of 0.2 and mixed before leaf infiltration. Moreover, a gene-silencing suppressor (HC-Pro) was added in BiFC assays as reported previously (62). The plants were kept in growth chambers in 16 h light at 25°C and 8 h dark at 22°C.

Membrane partitioning and immunoblotting analysis. Approximately 2 g of *N. benthamiana* leaves transiently expressing either GFP-p7B or each mutant protein were homogenized in lysis buffer containing 20 mM HEPES, pH 6.8, 150 mM potassium acetate, 250 mM mannitol, and 1 mM $MgCl_2$. Large cellular debris was removed by gentle centrifugation at 3,000 × *g* for 10 min, and the resulting supernatant was ultracentrifuged at 30,000 × *g* for 1 h to generate the soluble (S30) and the microsomal (P30) fractions. For chemical treatments, microsomal pellets were resuspended in 10 volumes of 100 mM Na_2CO_3 (pH 11), 4 M urea, lysis buffer containing 1% Triton X-100, or original lysis buffer. After incubation for 30 min on ice, the samples were centrifuged at 30,000 × *g* for 1 h. The resulting pellet was resuspended in lysis buffer. All fractions were analyzed by SDS-PAGE in 12% polyacrylamide gels and subsequently transferred to polyvinylidene difluoride (PVDF) membranes (GE Healthcare, Buckinghamshire, England) for immunoblotting with anti-GFP mouse polyclonal antibody (Roche Diagnostics GmbH, Mannheim, Germany).

Confocal laser scanning microscopy. *N. benthamiana* leaf tissue was mounted in water under a coverslip between 36 and 48 h following infiltration with *Agrobacterium* containing the required constructs. All imaging was conducted with a Leica TCS SL confocal laser scanning microscope using an HCX APO 40×/0.90 W water-dipping lens to study the subcellular localization of the fluorescence-tagged proteins. Enhanced green fluorescent protein (EGFP) and YFP fluorescence was visualized by 488-nm excitation with a Kr/Ar laser, and their emissions were examined with a band-pass filter for 500 to 530 nm. For imaging of cherry fluorescent protein (ChFP) and monomeric red fluorescent protein (mRFP) fluorescence, excitation at 514 nm (He/Ne laser) was used, whereas emission was observed at 600 to 620 (ChFP) and 550 to 590 (mRFP) nm. Sequential scanning was used to suppress optical cross talk between the fluorophores in stationary-structure colocalization assays. However, for dynamic structures, simultaneous scanning was employed to avoid green and red color misalignment.

Computer-assisted analysis of secondary structure and transmembrane helices. Prediction of transmembrane helices of MNSV p7B and mutant sequences was performed with Membrane Protein Explorer (MPEx) software version 3.0 (http://blanco.biomol.uci.edu/mpex/). The free-energy profile for membrane insertion of hydrophobic transmembrane proteins was estimated with Δ*G* Prediction Server v1.0 (http://www.cbr.su.se/DGpred/). Secondary-structure prediction of proteins was performed with SSPro 2.01 software (SYMPRED server [http://www.ibi.vu.nl/programs/sympredwww/]).

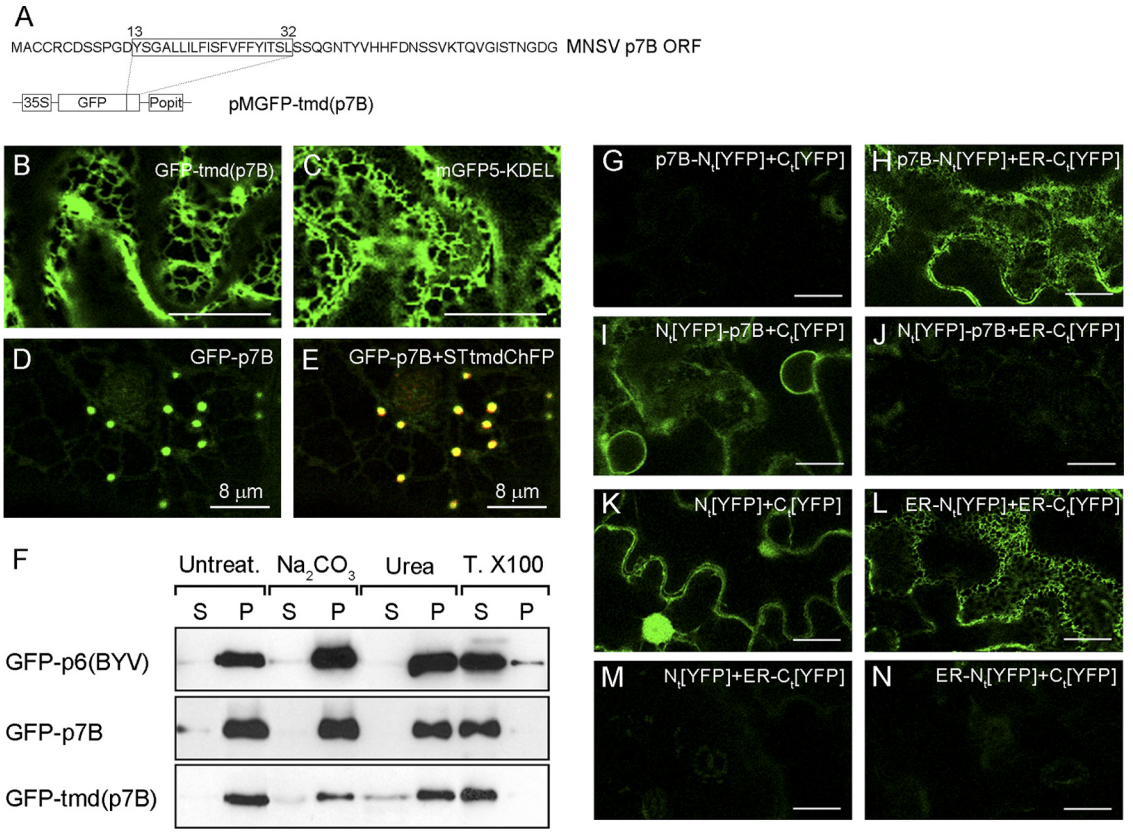

FIG. 1. Characterization of MNSV p7B topology in plant ER membranes. (A) ORF of MNSV p7B and schematic representation of the expression cassette in which amino acid sequence corresponding to the p7B computer-predicted TMD was cloned [pMGFP-tmd(p7B)]. 35S, *Cauliflower mosaic virus* 35S promoter. (B and C) Transient expression of GFP-tmd(p7B) (B) and the luminal ER marker, mGFP5-KDEL (C). A reticular staining pattern, which is indicative of ER localization, was observed in both proteins. (D and E) Colocalization of GFP-p7B (green channel) (D) and the Golgi apparatus-specific marker STtmdChFP (red channel) (not shown), and a merged image of both the green and red channels (E). The confocal microscopy images are representative of those taken in three independent experiments at 48 h postagroinfiltration. (F) Microsomal partitioning of tissue extracts from *N. benthamiana* leaves expressing GFP-p6(BYV), GFP-p7B, or GFP-tmd(p7B). After high-speed centrifugation, untreated pellets containing microsome (P) and supernatant (S) fractions were obtained. Alternatively, the P fraction was subjected to different treatments and separated again into S and P fractions by ultracentrifugation. Equivalent amounts of both untreated and treated S and P fractions were subjected to SDS-PAGE and analyzed by immunoblotting with anti-GFP antibodies. T. X100, Triton X-100. (G to N) Assessment of MNSV p7B orientation in plant ER membranes using a BiFC-based assay. The images (pseudocolored in green) correspond to single confocal microscopy scans obtained at 36 h postagroinfiltration in *N. benthamiana* leaves of the protein combinations indicated in the upper right of each panel. The silencing supressor HC-Pro was included in all coexpression assays. The scale bars correspond to 20 μm except where indicated.

RESULTS

Structural characteristics of the MNSV p7B hydrophobic domain. MNSV p7B is a single-pass membrane protein that inserts cotranslationally into the membrane of canine ER microsomes following a translocon-mediated pathway (40, 42). Depending on the computer-based method used, the p7B TMD length oscillates from 18 to 23 residues (data not shown), although all predictions share a consensus hydrophobic core from Y13 to L32 that mainly contains hydrophobic residues (A, I, V, L, and F) (Fig. 1A). The theoretical value calculated for the apparent free energy of the p7B TMD was negative enough ($\Delta G_{app} = -1.869$ kcal mol^{-1}) to be efficiently integrated into the ER membrane (25, 27) as previously reported (40).

The residue distribution and conformational preferences of the lateral chains determine the precise positioning of transmembrane helices in cellular membranes. Residues such as lysine, arginine, tryptophan, and tyrosine in membrane-buried helices often extend their side chains perpendicular to the membrane bilayer and point away from the hydrophobic core, generating a snorkeling effect (11). According to these observations, the side chain of the Y28 residue is expected to snorkel out of the p7B TMD hydrophobic core. In addition, analyses of TMDs from numerous membrane proteins have revealed that aromatic residues, in particular tyrosine, have a propensity to mainly locate at or near the lipid-water interface of the membrane (22, 35, 43). Therefore, the Y13 residue may reside at the p7B TMD helix end, where it favorably interacts with the cellular environment. Aromatic residues in this position have been referred to as "aromatic belts." Their functional significance is not known, although it has been speculated that aromatic belts perform an important function in membrane anchoring and stabilization of the corresponding protein (25). Finally, turn-promoting proline residues are excluded from the p7B TMD (26, 58).

Assessment of the MNSV p7B topology in plant ER membranes. To study the integration of p7B in plant cell ER membranes, the p7B TMD (Y13 to L32) was cloned as a carboxy-terminal fusion to the green fluorescent protein [GFP-tmd(p7B)] (Fig. 1A) and transiently expressed by agroinfiltration in *N. benthamiana* leaves. At 48 h postinfiltration, GFP-tmd(p7B) fluorescence appeared as an elaborate polygonal network (Fig. 1B) very reminiscent of that observed with mGFP5-KDEL, a luminal ER marker (Fig. 1C). Remarkably, GFP-tmd(p7B) was retained in the ER, while GFP-p7B was fully exported from the ER and located at cytoplasmic granules (Fig. 1D) that colocalized with Golgi stacks (Fig. 1E) (20). STtmdChFP, a Golgi-specific reporter consisting of the transmembrane domain of the rat α-2,6-sialyltransferase fused to the cherry fluorescent protein was used for this colocalization assay. The images in the report are representative of at least three independent experiments.

We also analyzed the association of GFP-tmd(p7B) with cellular membranes by subcellular fractionation. *N. benthamiana* tissue expressing GFP-tmd(p7B) was lysed, and extracts were separated by high-speed centrifugation into pellet (P30) and supernatant (S30) fractions. The P30 fraction was resuspended and divided into several aliquots, which were extracted with either 0.1 M Na_2CO_3 (pH 11), which would dislodge proteins entrapped within membrane structures; 4 M urea, which would dislodge proteins peripherically bound to the membrane; or Triton X-100, which would release integral membrane proteins. Control experiments were performed, including GFP-p7B fusion and *Beet yellows virus* p6 fused to GFP (GFP-p6) (20, 44). GFP-tmd(p7B), as well as GFP-p7B and GFP-p6 control proteins, behaved like typical integral membrane proteins because all of them were extracted from the membrane fraction only after incubation with Triton X-100 (Fig. 1F).

In vitro and *in vivo* assays using canine microsomal membranes and prokaryotic cells (*Escherichia coli*), respectively, revealed that p7B integrates into the ER membrane with an $N_{cytoplasm}$-C_{lumen} (N_{cyt}-C_{lum}) orientation (40). Since it has been shown that topological determinants of membrane proteins are affected by the lipid compositions of host membranes, which can differ among animal microsomes and the prokaryotic inner membrane and the ER membrane of plant cells (14), we studied *in vivo* the p7B membrane orientation in the plant ER. We employed a novel BiFC-based assay previously described for topology studies of both BYV p6 and the *Potato mop-top virus*-encoded integral membrane TGBp2 (62). This technique relies on the formation of a fluorescent complex between a fragment of the YFP targeted either to the cytoplasm or to the ER luminal space and a counterpart fragment fused to the integral membrane protein N or C terminus. When overexpressed, the two YFP halves interact, and therefore yield a fluorescent YFP, if they are located in the same subcellular compartment (62).

Amino-terminal and carboxy-terminal fusions of p7B to the N-terminal YFP fragment (p7B-N_t[YFP] and N_t[YFP]-p7B, respectively) were transiently coexpressed with the complementary C-terminal half of YFP, targeted either to the cytosol (C_t[YFP]) or to the ER lumen (ER-C_t[YFP]). Confocal microscopy analysis revealed that p7B-N_t[YFP] expression in the presence of either C_t[YFP] or ER-C_t[YFP] restored fluorescence, which clearly highlighted the ER network, only in the latter combination (Fig. 1G and H, respectively). According to the single-pass membrane status of p7B, the fluorescence was also observed when N_t[YFP]-p7B and C_t[YFP] were expressed together (Fig. 1I). No fluorescence was visible for the N_t[YFP]-p7B and ER-C_t[YFP] combination (Fig. 1J). After the coexpression of N_t[YFP] and C_t[YFP], fluorescence was observed in the cytoplasm and nuclei (Fig. 1K), indicating that the expression level of each split YFP fragment was sufficient to allow fluorescence complementation (62). Alternatively, fluorescence was confined to the ER network after the coexpression of ER-N_t[YFP] and ER-C_t[YFP] (Fig. 1L), indicating that both proteins were properly targeted to the ER lumen (62). The coexpression of N_t[YFP] and ER-C_t[YFP] or the ER-N_t[YFP] and C_t[YFP] combination resulted in no fluorescence detection, indicating that each YFP split fragment was fully located in the appropriate subcellular compartment (Fig. 1M and N, respectively). Taken together, our observations indicate that in plant cells, as occurs in heterologous systems, the N-terminal region of p7B (residues 1 to 12) is exposed to the cytoplasm whereas the C-terminal domain (residues 33 to 60) faces the ER luminal side (type II topology).

Contribution of the p7B topology determinants to MNSV cell-to-cell movement. To assess the relevance of p7B topology determinants in MNSV cell-to-cell movement, a series of site-directed mutations was introduced into the p7B ORF of the pMNSV(Al)-Δcp-GFP clone (Fig. 2A), from which infectious transcripts expressing free GFP can be obtained (18). Wild-type (Fig. 2B) and mutant (Fig. 2C to U and Table 1) MNSV RNAs were inoculated into the cotyledons of melon plants, and the local spread of infection was measured by quantifying the fluorescent area. The results are presented according to the p7B topological determinant affected.

(i) Mutations affecting p7B TMD hydrophobicity. Since the most prominent p7B topological determinant is the Y13-L32 hydrophobic region (28, 61), different mutations were directed to modify TMD hydrophobicity. An amino acid replacement strategy was used instead of amino acid deletion/insertion to preserve the p7B TMD length (see Table S2 in the supplemental material) because the distribution of single-pass membrane proteins along the organelles of the secretory pathway depends on their TMD length (7). Hydrophobicity was reduced by engineering different alanine replacements (A replacements) of hydrophobic V, L, and I, as well as of aromatic F and Y residues, which were positioned between residues S14 and L32 (5). A replacements, which were initially made in groups of three, led to a 0.6- to 4-fold reduction of wild-type TMD hydrophobicity (Table 1). The TMD hydrophobicity of each mutant was measured as free energy for membrane insertion using the "biological" scale determined by Hessa et al. (25). Upon inoculation, all the triple mutants were completely arrested to single, initially infected cells (Fig. 2C to F and Table 1).

Considering that a hydrophobicity threshold is required for accurate integration of TMDs, we evaluated the relationship of this phenomenon with MNSV cell-to-cell movement. For this purpose, p7B TMD hydrophobicity was progressively reduced by introducing double or single A replacements into the S14-L32 hydrophobic region. All mutants showing TMD free energies higher than -1.191 kcal mol^{-1} (obtained with the

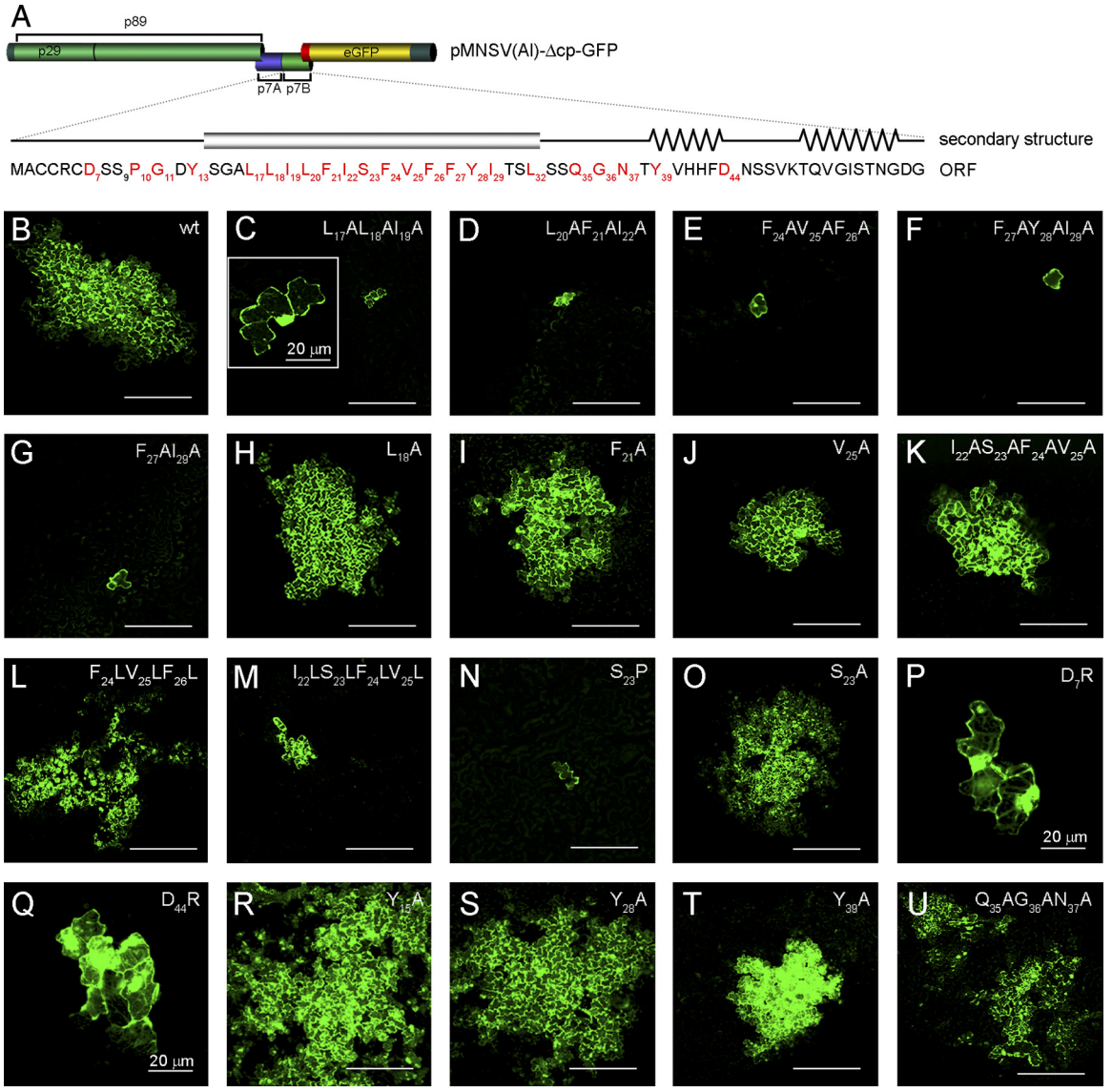

FIG. 2. Contribution of p7B topological determinants in viral cell-to-cell movement. (A) Schematic representation of the recombinant infectious clone pMNSV(AI)-Δcp-GFP, in which MNSV CP was replaced by the GFP gene. A secondary-structure illustration and the ORF of p7B are shown below. Viral and fluorescent protein names are indicated. The conserved α-helix/transmembrane domain and β-sheet structures are represented by a box and jagged lines, respectively. MNSV p7B residues affected by mutations are shown in red. The subscript numbers indicate protein residue positions. (B to U) Confocal microscopy scans taken at 2 to 3 days postinoculation of both wild-type and mutant RNAs in melon plant cotyledons. The images are representative of infection foci observed in three independent experiments. Viral RNAs were generated by *in vitro* transcription of the corresponding pMNSV(AI)-Δcp-GFP variant. Mutations are indicated in the upper right of each panel. The scale bars correspond to 200 μm except where indicated.

$F_{27}AI_{29}A$ mutant) (Fig. 2G and Table 1) were competent in cell-to-cell movement, although the infected area was slightly reduced (Fig. 2H to J and Table 1) compared with wild-type RNA cell-to-cell movement (Fig. 2B). To segregate the putative adverse effect in the cell-to-cell movement generated by introducing multiple mutations into the p7B TMD from that produced by the TMD hydrophobicity reduction itself, another p7B mutant was obtained in which positions 22 through 25 were replaced with alanines (the $I_{22}AS_{23}AF_{24}AV_{25}A$ mutant). The resulting ΔG_{app} was similar to that obtained with the $L_{18}A$ mutant (-1.465 kcal mol^{-1} versus -1.472 kcal mol^{-1}, respectively). Interestingly, this mutant was functional in viral cell-to-cell movement (81% of the local movement in relation to the wild-type RNA) (Fig. 2K and Table 1).

In addition, the effect of increasing p7B TMD hydrophobicity in cell-to-cell movement was also assessed. For this purpose, positions 24 through 26 were altered to leucines instead of to alanines (the $F_{24}LV_{25}LF_{26}L$ mutant) to slightly increment TMD hydrophobicity (ΔG_{app} [3L] = -2.383 versus ΔG_{app} [wt] = -1.869 kcal mol^{-1}) (Table 1). In contrast to the $F_{24}AV_{25}AF_{26}A$ mutant, this modification apparently had no effect on cell-to-cell movement (Fig. 2L and Table 1). However, a 2-fold increment of TMD hydrophobicity, which was obtained by replacing positions 22 through 25 with leu-

TABLE 1. p7B mutations set into structural feature groups and summary of results obtained in cell-to-cell movement assays and subcellular localization experiments

Mutation	Structural feature	ΔG_{app} (kcal mol^{-1})	Movement (%)	Subcellular localization[a]		
				ER	GA	Pd
wt		−1.869	100	+	+	+
$L_{17}AL_{18}AI_{19}A$	TMD hydrophobicity	−0.493	0	+	−	−
$L_{20}AF_{21}AI_{22}A$		−0.408	0	+	−	−
$F_{24}AV_{25}AF_{26}A$		−0.878	0	NA	NA	NA
$F_{27}AI_{29}AL_{32}A$		−0.916	0	NA	NA	NA
$F_{27}AY_{28}AI_{29}A$		−1.164	0	NA	NA	NA
$F_{27}AI_{29}A$		−1.191	0	+	−	−
$I_{22}AS_{23}AF_{24}AV_{25}A$		−1.465	81	+	+	+
$L_{18}A$		−1.472	72	+	+	+
$F_{21}A$		−1.563	86	+	+	+
$V_{25}A$		−1.682	66	+	+	+
$F_{24}LV_{25}LF_{26}L$		−2.383	87	+	+	+
$I_{22}LS_{23}LF_{24}LV_{25}L$		−3.630	9.7	+	−	−
$Q_{35}AG_{36}AN_{37}A$	Triple-mutant control	−1.869	80	+	+	+
D_7R	Net balance charge	−1.869	12	+	−	−
$D_{44}R$		−1.869	16	+	−	−
$Y_{13}A$	Aromatic residues	−1.725	154	+	+	+
$Y_{28}A$		−1.842	123	+	+	+
$Y_{39}A$		−1.869	54	+	+	+
$S_{23}P$	α-helix	−1.384	0	+	+	−
$S_{23}A$	Control Ser23	−2.598	93	+	+	+

[a] +, present; −, absent; NA, not assayed.

cines (ΔG_{app} [4L] = −3.630 versus ΔG_{app} [wt] = −1.869 kcal mol^{-1}), drastically reduced viral movement (9.7%) (Fig. 2M and Table 1). As expected, given the fact that residues I, L, V, F, and A, in decreasing order, display the highest α-helix propensities in a nonpolar environment (36), computer predictions obtained using the SSPro 2.01 software (SYMPRED server) and MPEx software version 3.0, respectively, show that the α-helix conformation and the TM length of the p7B TMD are not disturbed by mutations (see Table S2 in the supplemental material). A feasible conclusion that could be drawn from these results is that an appropriate p7B TMD hydrophobicity value is required for MNSV cell-to-cell movement.

(ii) Mutations affecting p7B TMD secondary structure. To test whether the p7B TMD secondary structure was relevant in MNSV cell-to-cell movement, the $S_{23}P$ mutant was constructed. Statistical studies have revealed that α-helical membrane-buried regions of nonchannel proteins are largely devoid of intramembrane proline residues (13). The cyclic structure of this amino acid strongly restricts the conformational space, resulting in a redirection of the peptide chain that can distort α-helix structures (13). According to this observation, the $S_{23}P$ mutation abolished MNSV cell-to-cell movement (Fig. 2N and Table 1), whereas only a slight reduction in local spread was observed when the same serine was changed to alanine (Fig. 2O and Table 1). Thus, structural requirements are also critical for efficient MNSV cell-to-cell movement.

(iii) Mutations affecting the net charge distribution on either side of the p7B TMD. The membrane orientation of transmembrane proteins is primarily determined by the net charge balance in the 13 to 25 residues flanking both sides of the TMD, whereby the more positive end is predominantly positioned on the cytoplasmic side of the membrane. This phenomenon is known as the "positive-inside rule" (34). Since p7B shows identical net charge balances (−1) on either side of the TMD, we decided to obtain the D_7R and $D_{44}R$ mutants, which resulted in a negative-to-positive inversion of the net charge balance (−1 to +1) in the N_t and C_t regions, respectively, to study the contribution of the positive-inside rule in MNSV cell-to-cell movement. Despite the D_7R and $D_{44}R$ mutations possibly favoring wild-type and opposite p7B membrane orientations, respectively, cell-to-cell movement was drastically reduced in both cases (10 to 15%) (Fig. 2P and Q, respectively, and Table 1).

(iv) Mutations affecting p7B aromatic residues. To study the implications of residues Y13 (the putative "aromatic belt") and Y28 (the putative snorkeling effector) in MNSV cell-to-cell movement, we constructed the $Y_{13}A$ and $Y_{28}A$ mutants. Unexpectedly, the infected fluorescent areas of both mutants were greater than that obtained with wild-type RNA (Fig. 2R and S, respectively, and Table 1), whereas a one-half reduction of the local movement relative to the wild type was observed in the $Y_{39}A$ mutant. The location of the residue Y39 in a conserved β-sheet conformation (42), which might be involved in alternative functions that are also relevant in cell-to-cell movement, could explain the discrepancies observed (Fig. 2T and Table 1). In this sense, the $Q_{35}AG_{36}AN_{37}A$ mutation, located downstream of the TMD but not affecting the conserved region, produced only a 20% reduction in local movement relative to the wild type (Fig. 2U and Table 1).

Distortion of the TMD secondary structure is the unique topological determinant affecting p7B membrane association. In order to study whether the different topological determinants analyzed above affect p7B membrane association, four representative mutants were analyzed. The selected mutants included (i) either the $L_{20}AF_{21}AI_{22}A$ or $I_{22}LS_{23}LF_{24}LV_{25}L$ mutation, which brought about the greatest reduction or increase in TMD hydrophobicity, respectively; (ii) the $D_{44}R$ mutation, which generates a positive net charge balance in the

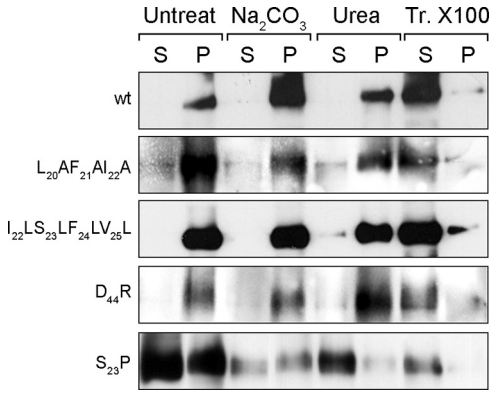

FIG. 3. Membrane association analysis of GFP-p7B mutants. Extracts from *N. benthamiana* leaves expressing GFP-p7B, GFP-p7B($L_{20}AF_{21}AI_{22}A$), GFP-p7B($I_{22}LS_{23}LF_{24}LV_{25}L$), GFP-p7B($D_{44}R$), or GFP-p7B($S_{23}P$) were separated into pellet (P) and supernatant (S) fractions by high-speed centrifugation (untreated fractions). The P fractions were divided into several aliquots and treated either with 0.1 M Na_2CO_3 (pH 11)-4 M urea or 1% Triton X-100 plus 0.5 M NaCl (Tr. X100). Samples were again separated into S and P fractions by ultracentrifugation. Equivalent amounts of untreated and treated S and P fractions were subjected to SDS-PAGE and analyzed by immunoblotting with anti-GFP antibodies.

p7B C-terminal domain; and finally, (iii) the $S_{23}P$ mutation, which most likely distorts the membrane-spanning α-helix. All four mutations were individually introduced into the GFP-p7B binary construct and transiently expressed in *N. benthamiana* leaves. The membrane association status of mutant MPs was characterized by subcellular fractionation, followed by different treatments as described previously. Neither the $L_{20}AF_{21}AI_{22}A$, the $I_{22}LS_{23}LF_{24}LV_{25}L$, or the $D_{44}R$ mutation had an effect on membrane association, given that the segregation between the S and P fractions of mutant MPs was like that of wild-type p7B (Fig. 3). With the $S_{23}P$ mutant, the subcellular fractionation analysis revealed that a significant fraction of the protein (more than 50% of the signal) was recovered in the soluble fraction with no solubilization treatment (Fig. 3). Moreover, the $S_{23}P$ mutant fraction that remained associated with the membrane behaved like peripheral membrane proteins because it was partially and fully extracted with alkaline and 4 M urea solutions, respectively (Fig. 3).

Next, we introduced the above-mentioned mutations into the binary constructs expressing either N_t[YFP]-p7B or p7B-N_t[YFP] to study membrane orientation. It had been previously demonstrated that the N terminus of a membrane protein is inserted first into the translocon (21). Thus, very hydrophobic TMDs leave no time for N-terminal reorientation, resulting in N_{lum}-C_{cyt} orientation, whereas less hydrophobic TMDs delay their translocon exit, leaving open the possibility of reorientation of the N terminus (21). In this scenario, the $L_{20}AF_{21}AI_{22}A$ and $I_{22}LS_{23}LF_{24}LV_{25}L$ mutants favor wild-type and opposite orientations, respectively. However, both mutants adopted the wild-type orientation, since ER fluorescence was observed when the corresponding p7B-N_t[YFP] and N_t[YFP]-p7B mutants were coexpressed with ER-Ct[YFP] and Ct[YFP], respectively (Fig. 4A and D for the $L_{20}AF_{21}AI_{22}A$ mutant and 4E and H for the $I_{22}LS_{23}LF_{24}LV_{25}L$ mutant). Fluorescence was not observed in the opposite combinations (Fig. 4B and C for the $L_{20}AF_{21}AI_{22}A$ mutant and Fig. 4F and

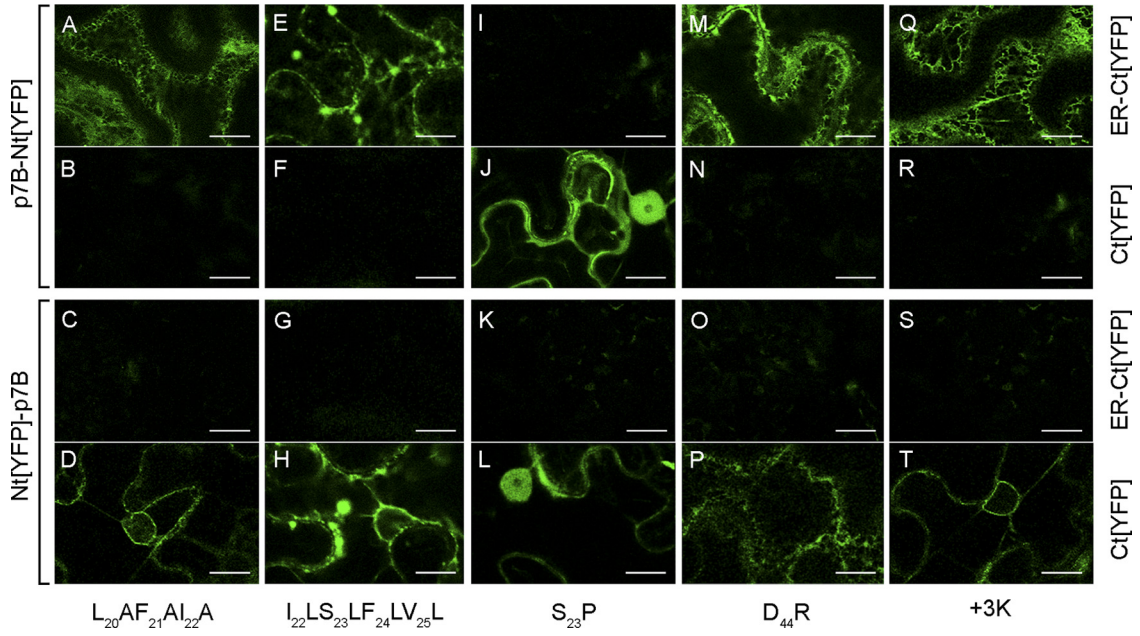

FIG. 4. Membrane orientation analysis in plant ER membranes of the p7B($L_{20}AF_{21}AI_{22}A$) (A to D), p7B($I_{22}LS_{23}LF_{24}LV_{25}L$) (E to H), p7B($S_{23}P$) (I to L), p7B($D_{44}R$) (M to P), and p7B(+3K) (Q to T) mutants using a BiFC-based assay. The images correspond to single confocal microscopy scans obtained 36 h post agroinfiltration in *N. benthamiana* leaves of the following construct combinations: the top and second rows correspond to coexpression of p7B-Nt[YFP] mutants with either ER-Ct[YFP] or Ct[YFP], respectively; the third and fourth rows correspond to coexpression of Nt[YFP]-p7B mutants with either ER-Ct[YFP] or Ct[YFP], respectively. Mutations are indicated under each column. The silencing supressor HC-Pro was included in all coexpression assays. The scale bars correspond to 20 μm. The images are pseudocolored in green.

G for the $I_{22}LS_{23}LF_{24}LV_{25}L$ mutant). On the other hand, either p7B(S_{23}P)-N_t[YFP] or N_t[YFP]-p7B(S_{23}P), together with Ct[YFP], resulted in both nuclear and cytoplasmic fluorescence (Fig. 4J and L, respectively), most likely as a consequence of the presence of a soluble fraction of the S_{23}P mutant, supporting the results previously observed in the microsomal-partitioning assay (Fig. 3). No fluorescence was visible with the p7B(S_{23}P)-N_t[YFP] and ER-Ct[YFP] combination, indicating that the C-terminal region of p7B(S_{23}P)-N_t[YFP] is not translocated into the ER lumen (Fig. 4I).

The contribution of the positive-inside rule to p7B membrane orientation was assessed in both the D_{44}R mutant and the +3K insertion mutant, which contains three extra lysine residues after the S32 position. Despite the fact that both mutant proteins should adopt a wild-type opposite orientation according to the positive-inside rule, no topology inversion was observed (Fig. 4M to P for the D_{44}R mutant and Fig. 4Q to T for the +3K mutant). These results contrast with those previously reported in a prokaryotic system, where topology inversion of an MNSV p7B-GFP recombinant protein harboring the +3K insertion was achieved (40). This discrepancy may be due to several factors: (i) differences in the compositions of the anionic phospholipids between the *E. coli* inner membrane and the ER membrane of plant cells, (ii) the absence of electrochemical potential in plant ER membranes, and (iii) the possibility that different solutions to membrane insertion operate in different organisms.

Therefore, only the disruption of the TMD secondary structure producing an alteration of the p7B membrane topology might explain the previously observed cell-to-cell movement inhibition. However, since the topology of p7B was not substantially affected in the remaining mutants, no direct correlation between a noncompetent cell-to-cell movement phenotype and appropriate p7B insertion in the ER membrane can be drawn. These results suggest that other factors influencing the functionality of p7B in viral movement were affected in these mutants.

Trafficking of p7B to the cell periphery is affected at different stages in noncompetent movement mutants. Several studies have identified aromatic, charged, and hydrophobic residues, in addition to TMD hydrophobicity, as structural determinants controlling the intracellular trafficking of proteins (4, 10). Thus, those mutations which were initially engineered to modify p7B topology may have also affected the ER-GA-Pd pathway followed by p7B to reach the Pd (20). To test this possibility, we introduced both competent and deficient movement mutations into the GFP-p7B recombinant protein. Agrobacterium-mediated transient expression was used to examine the subcellular localization of GFP-p7B mutants in *N. benthamiana* leaves. Until 36 h postagroinfiltration, expression of all mutant proteins resulted in a reticular staining pattern characteristic of ER localization (Fig. 5A and Table 1). Strong ER labeling was observed, except for GFP-p7B(S_{23}P), which faintly labeled this cellular compartment (scanning of this mutant used a higher laser intensity than the rest).

At 48 h postagroinfiltration, ER labeling was scarcely observed, except for GFP-p7B($I_{22}LS_{23}LF_{24}LV_{25}L$). In this case, the ER staining underwent morphological changes, leading to the conversion of the tubular ER pattern into small cytoplasmic bodies that collapsed into large aggregates (Fig. 5B and 6G). Similar behavior was previously reported for TMV MP (45). When transiently expressed together in *N. benthamiana* leaves, TMV MP-mRFP and GFP-p7B($I_{22}LS_{23}LF_{24}LV_{25}L$) colocalized in the same ER aggregates (Fig. 5C), indicating that GFP-p7B($I_{22}LS_{23}LF_{24}LV_{25}L$) induces rearrangements of the plant ER membranes, in contrast to GFP-p7B (wt). One possibility is that the $I_{22}LS_{23}LF_{24}LV_{25}L$ mutation retained the protein in the ER membrane and that ER aggregates were an experimental artifact caused by its overexpression. In marked contrast, the remaining mutants were mostly localized in motile cytoplasmic vesicles (Fig. 6). These structures were visualized in colocalization with the GA marker STtmdChFP, but only when mutants were competent for virus movement (Fig. 6A, B, D, F, I, J, and K and Table 1). One exception was the S_{23}P mutant, which associated with the Golgi marker, but the corresponding viral RNA did not move (Fig. 6H and Table 1).

Localization of MP to the GA appears to be important for virus movement, but it is not sufficient for this activity. To further analyze whether the p7B post-Golgi transport to Pd was affected, we transiently coexpressed GFP-p7B (Fig. 7A) and the different mutants (Fig. 7B to J) with the PNRSV MP, a Pd marker (2). GFP-p7B harboring competent movement mutations (Fig. 7C, D, E, H, and I and Table 1) generated fluorescent peripheral punctate structures that colocalized with the Pd marker. In contrast, GFP-p7B, harboring noncompetent movement mutations, including GFP-p7B(S_{23}P), was not localized to Pd (Fig. 7B, F, G, and J and Table 1). Overall, these data indicate that the mutations inhibiting virus cell-to-cell movement affect the intracellular pathway of p7B to the cell periphery at different stages, including ER exit, GA targeting, and post-Golgi apparatus transport.

DISCUSSION

The final topology of membrane proteins is determined by a set of intricate interactions between the structural determinants of the protein, which are recognized by the translocon complex, and the particular properties of the destination membrane. These properties include the lipid composition, cholesterol concentration, membrane thickness, and electrochemical potential (6, 14). Host-specific chaperones, such as TRAM, may also be required for membrane insertion of viral MPs (50). The high variability of these properties among different organisms emphasizes the importance of studying membrane protein structure-function relationships in the native lipid environment context. In this work, live-cell fluorescence imaging was performed to investigate the topology of MNSV p7B, a plant virus MP, in the ER membranes of plant cells. MNSV p7B has been previously shown to integrate cotranslationally into both canine pancreas microsomes and the *E. coli* inner membrane with an N_{cyt}-C_{lum} orientation (40, 42). We also demonstrated that the GFP-p7B fusion was able to integrate into the plant ER membrane. Nevertheless, information about the contribution of the hydrophobic region to the process and about the orientation of the viral MP in the membrane is lacking (20).

The results presented here reveal that the p7B TMD can promote efficient ER targeting and strong association of GFP with ER membranes, thus acting as an ER-targeting domain in plant cells. Although the plant GA has been reported to be the possible default destination for single-pass membrane proteins

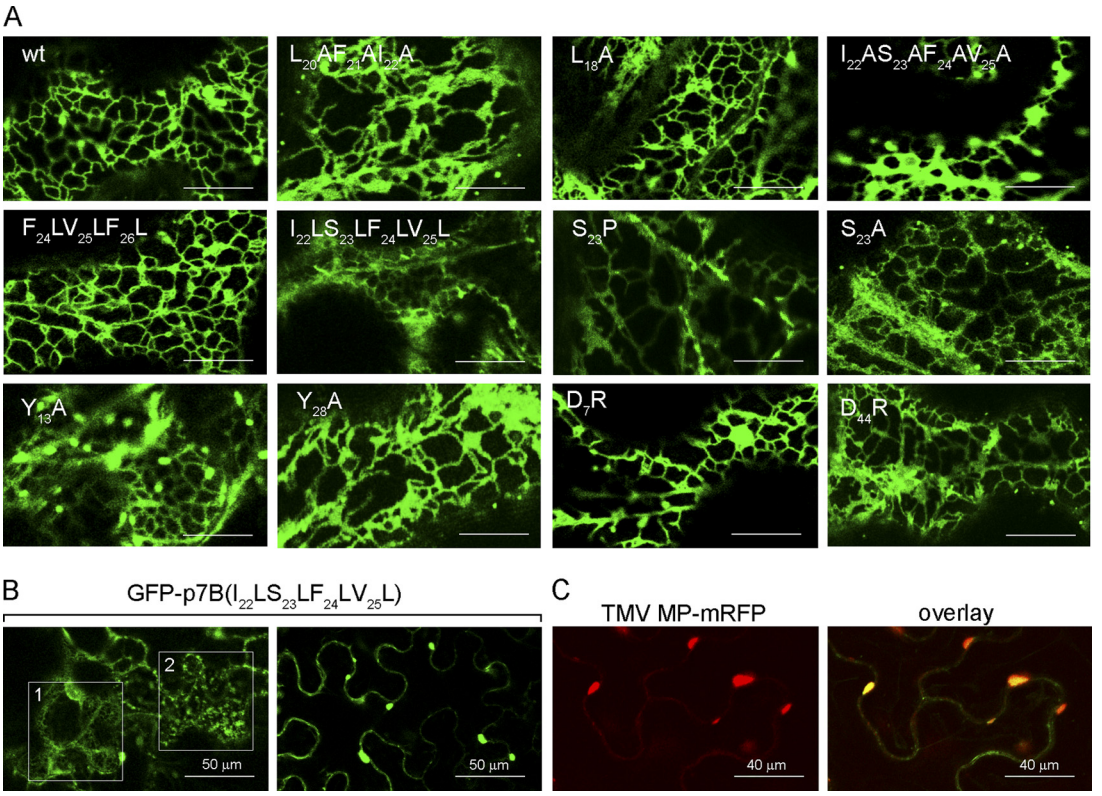

FIG. 5. (A) Subcellular localization of the wild type and mutants of GFP-p7B in the ER. Confocal microscopy scans were taken at 36 h postagroinfiltration in *N. benthamiana* leaves. The scale bar corresponds to 15 μm. A complete review of the results can be found in Table 1. Mutations are indicated in the upper left of each image. (B) Confocal images of *N. benthamiana* epidermal cells expressing GFP-p7B($I_{22}LS_{23}LF_{24}LV_{25}L$) taken at 48 h postagroinfiltration. The images show how ER staining obtained after GFP-p7B($I_{22}LS_{23}LF_{24}LV_{25}L$) expression underwent morphological changes leading to the conversion of the tubular ER pattern (the region enclosed in square 1 on the left) into small cytoplasmic bodies (the region enclosed in square 2 on the left) that collapsed into large aggregates (right). (C) Colocalization of TMV MP-mRFP (left) and GFP-p7B($I_{22}LS_{23}LF_{24}LV_{25}L$) (not shown) into ER aggregates at 48 h postagroinfiltration in *N. benthamiana* leaves. The merged image of green and red channels is shown on the right.

containing TMDs about 19 to 20 amino acids in length (7), the p7B TMD by itself was unable to promote GFP transport from the ER to the GA, resulting in ER retention. Thus, MNSV p7B export from the ER appears to be controlled by specific export motifs located in the cytoplasmic and/or luminal domain. In the absence of these dominant motifs, ER retention may result from a better match between the lipid composition of the ER membrane and p7B TMD length/hydrophobicity. The p7B TMD clearly differs from the TMD of the plasmodesmata-located protein PLPd1a, since the latter domain contains all the information required for the intracellular transport of heterologous proteins to Pd via the secretory pathway (56). Characterization of putative p7B ER export signals will be the subject of further investigation, since the p7B ORF does not contain any of the classical ER export sequences identified in single-spanning membrane proteins (4). A similar situation has been recently reported for the rice secretory carrier membrane protein 1 (SCAMP1), for which the ER export signal is apparently unique (10).

On the other hand, there are many p7B structural properties that could participate in establishing its final topology. Among them, the more prominent are the length, hydrophobicity, and α-helix configuration of the TMD, as well as the net balance charge of the extramembrane TMD-proximal regions. For efficient insertion into the lipid bilayer, protein transmembrane segments require a minimum hydrophobicity threshold, which must be markedly high for ER-targeting sequences like the p7B TMD (38). According to this assumption, a 2-fold reduction of p7B TMD hydrophobicity was sufficient to eliminate cell-to-cell movement. Similar results were also obtained for the $I_{22}LS_{23}LF_{24}LV_{25}L$ mutant, whose thermodynamic properties for membrane insertion proved more favorable than that of the wild-type sequence, strongly suggesting the need for an appropriate hydrophobicity value for the p7B function in cell-to-cell movement. Intriguingly, both the insertion and membrane orientation of the $L_{20}AF_{21}AI_{22}A$ and $I_{22}LS_{23}LF_{24}LV_{25}L$ mutants, with the most reduced and increased TMD hydropathy, respectively, were apparently not affected. Moreover, noncompetent mutations that either lower or increase TMD hydrophobicity strongly correlate with either incorrect intracellular targeting to unidentified cytoplasmic vesicles or a drastic rearrangement of ER membranes, respectively, which impeded the ability of p7B to access the Pd. It is well known that plant viruses need to exploit Pd to move from cell to cell in a process in which virus-encoded movement proteins play a central role. Therefore, the ability of p7B to function in viral movement most likely depends on Pd localization, which is defective in noncompetent cell-to-cell movement phenotypes.

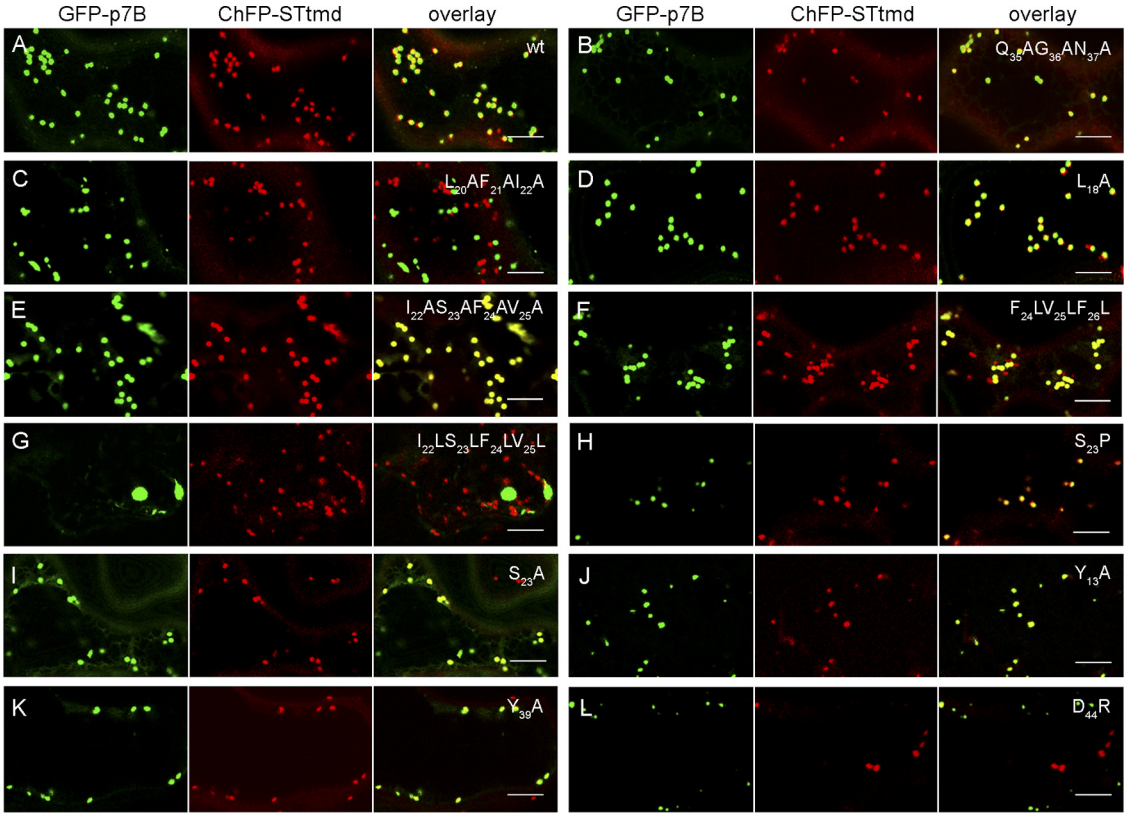

FIG. 6. Coexpression of the wild type and mutants of GFP-p7B (GFP-p7B) with the GA marker STtmdChFP (STtmdChFP). Merged images of the green and red channels are shown on the right (overlay). The confocal images correspond to coexpression of the GA marker with either the wild-type GFP-p7B (A), the $Q_{35}AG_{36}AN_{37}A$ mutant (B); the $L_{20}AF_{21}AI_{22}A$, $L_{18}A$, $I_{22}AS_{23}AF_{24}AV_{25}A$, $F_{24}LV_{25}LF_{26}L$, or $I_{22}LS_{23}LF_{24}LV_{25}L$ mutant affecting p7B TMD hydrophobicity (C to G, respectively); the $S_{23}P$ mutant affecting the α-helix structure of the p7B TMD (H); the $S_{23}A$ mutant used as a control for the $S_{23}P$ mutant (I); the $Y_{13}A$ mutant lacking the Y13 putative aromatic belt (J); the $Y_{39}A$ mutant affecting the conserved β-sheet structure at the p7B C-terminal domain (K); or the $D_{44}R$ mutant displaying a C-terminal bias for positively charged amino acids (L). Mutations are indicated in the overlay panels. The confocal microscopy scans were taken 48 h after agroinfiltration. The scale bars correspond to 8 μm. A complete review of the results can be found in Table 1.

We can conclude that the p7B TMD controls the insertion of the MP into the ER membrane and can also modulate the next cellular destination of the MP in the presence of the ER export motifs located in the cytoplasmic and/or luminal domain.

There are three different TMD determinants controlling the subcellular localization of a membrane protein: the length of the TMD, the presence of specific sequence elements, and the overall hydrophobic profile (7, 9, 56). We found that the length of the predicted p7B TMD was unaffected by mutations and that the p7B TMD itself was unable to transport GFP out of the ER. Therefore, other biophysical features of the TMD, such as the overall hydrophobicity profile, modulate the proper targeting of the MP. Accordingly, changes in the hydropathy profile of the TMD present in ER-resident cytochrome P450 2C1 also cause mislocation to different subcellular compartments in COS1 cells (54). Moreover, the sarcolemmal membrane-associated protein (SLMAP) possesses two alternatively spliced transmembrane regions (tail anchor TA1 or TA2); TA2 is less hydrophobic than TA1 and determines the subcellular localization of the SLMAP in the mitochondria, while SLMAP TA1 is targeted to the ER. However, the TA2-4L mutant has a transmembrane region that is only slightly less hydrophobic than the wild-type TA1, and it shares similar TA1-targeting properties (9). It is tempting to speculate that large variations below or above wild-type p7B TMD hydrophobicity affect the balance between TMD-membrane lipid interaction and signal-mediated export, resulting in different outcomes depending on TMD strength. For example, p7B ER retention dictated by the strong TMD hydrophobicity of the $I_{22}LS_{23}LF_{24}LV_{25}L$ mutant predominated over the p7B ER export signals located in the extramembrane domains. Addition of a diacidic export motif suppresses the ER retention of the *Yellow fever virus* (YFV) E envelope protein that is mediated by a TMD, but the same tagging did not override the ER retention signal of the TMD from the YFV prM envelope protein (12).

Although many transmembrane α-helices contain bends and other distortions that have important implications for protein function (47, 58), the proline-induced kink resulting from the $S_{23}P$ mutation substantially affected the topology and intracellular transport of p7B, as well as viral cell-to-cell movement. The effect of the S23P mutation on MP membrane insertion was most likely due to the central position of the proline within the TMD (25). The distorted helix was likely too short to be well accommodated in the hydrophobic core of the ER membrane, generating a negative hydrophobic mismatch. In this situation, transmembrane helices can adopt a surface orienta-

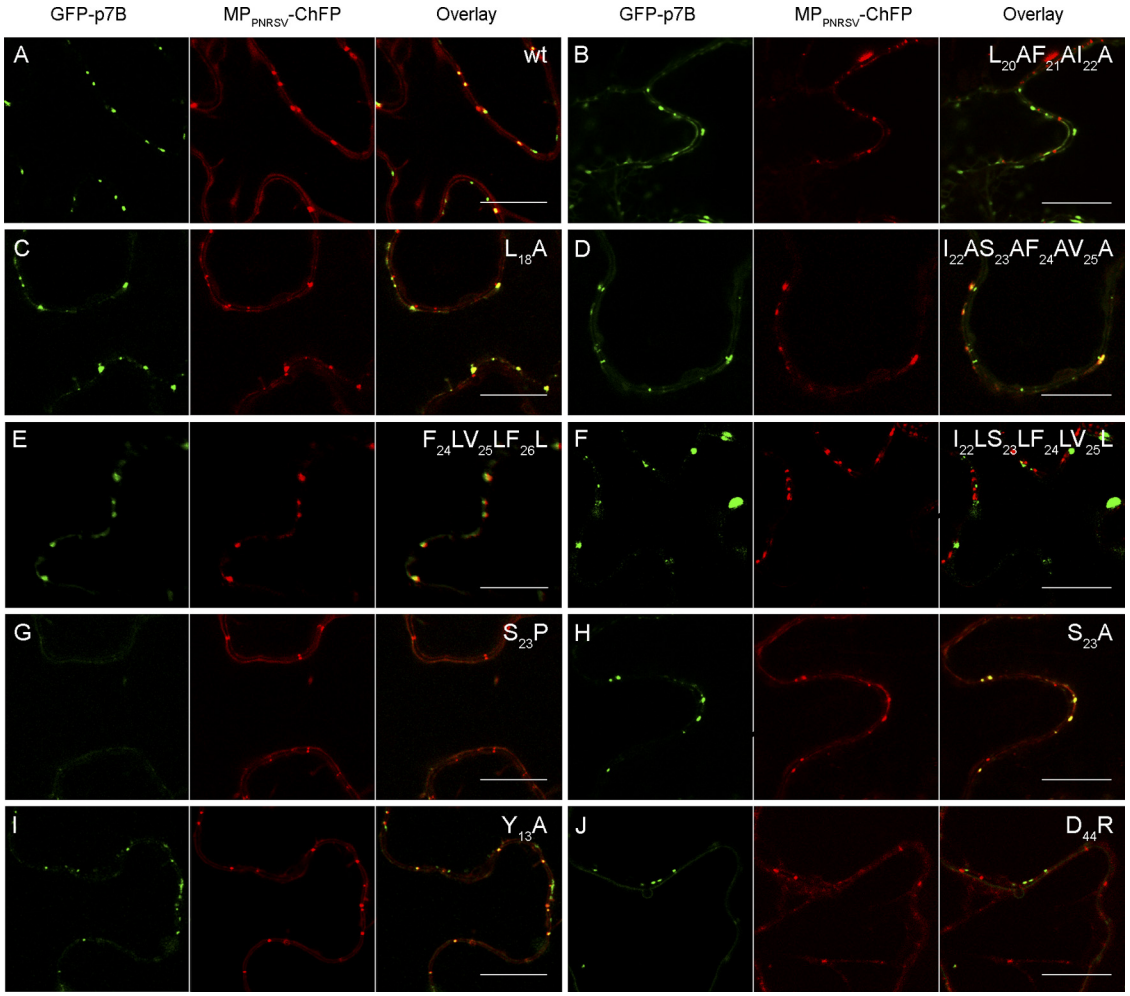

FIG. 7. Coexpression of the wild type and mutants of GFP-p7B (GFP-p7B) with the plasmodesmata marker PNRSV MP-ChFP (PNRSV MP-ChFP). Merged images of green and red channels are shown on the right (overlay). The confocal images correspond to coexpression of the Pd marker with either the wild-type GFP-p7B (A); the $L_{20}AF_{21}AI_{22}A$, $L_{18}A$, $I_{22}AS_{23}AF_{24}AV_{25}A$, $F_{24}LV_{25}LF_{26}L$, or $I_{22}LS_{23}LF_{24}LV_{25}L$ mutant affecting p7B TMD hydrophobicity (B to F, respectively); the $S_{23}P$ mutant affecting the α-helix structure of the p7B TMD (G); the $S_{23}A$ mutant used as a control for the $S_{23}P$ mutant (H); the $Y_{13}A$ mutant lacking the Y13 putative aromatic belt (I); or the $D_{44}R$ mutant displaying a C-terminal bias for positively charged amino acids (J). Mutations are indicated in the overlay panels. The scale bars correspond to 8 μm. The confocal microscopy scans were taken 48 h after agroinfiltration. A complete review of the results can be found in Table 1.

tion rather than a membrane-inserted state, as occurred in the $S_{23}P$ mutant (46). Unexpectedly, this weak membrane association was sufficient to promote ER-to-GA transport but not post-Golgi apparatus targeting to Pd. This indicates that membrane insertion is essential for the p7B function in virus movement.

It is largely accepted that charged residues flanking the hydrophobic stretch strongly modulate protein orientation relative to the membrane. A positive-inside rule seems to apply universally to all the integral membrane proteins, by which positively charged residues are predominantly found in the flanking sequence that remains exposed to the cytosol. Our results showed that p7B always adopts a N_{cyt}-C_{lum} orientation *in planta*, although no biased distribution of positively charged residues between cytoplasmic and ER luminal segments was observed. Mutations that violate the positive-inside rule can prevent the insertion of a TMD. However, p7B was efficiently inserted into the ER membrane in the correct membrane orientation when a negative-to-positive inversion of the Ct domain net charge was obtained in both the $D_{44}R$ and the +3K mutants. A similar override of the positive-inside rule has been described for the polytopic channel that constitutes the ductin protein and mitochondrial inner membrane proteins (15, 17). The critical contribution of charged residues to intracellular transport of p7B and MNSV cell-to-cell movement is most likely related to its involvement in interactions with host and/or viral factors. Interestingly, point mutations affecting charged residues introduced into ER luminal or cytosolic segments of BYV p6 resulted in a drastic reduction of cell-to-cell movement (44). However, neither the topology nor the subcellular localization of these BYV p6 mutants was studied.

The orientation of proteins in membranes can also be controlled by both TMD length and hydrophobicity. Long and very hydrophobic TMDs favor translocation of the N terminus across ER membranes (N_{lum}-C_{cyt} orientation), whereas short and less hydrophobic segments adopt an N_{cyt}-C_{lum} topology.

However, a 2-fold increase in the TMD hydrophobicity of wild-type p7B (the $I_{22}LS_{23}LF_{24}LV_{25}L$ mutant) did not result in the opposite membrane orientation. BYV p6 is structurally very similar to MNSV p7B, but it shows an N_{lum}-C_{cyt} orientation in plant ER membranes. BYV p6 exhibits a positive-charge bias (+2) for the cytoplasmic Ct domain, and its TMD is longer (23 residues) and more hydrophobic ($\Delta G_{app(p6)} = -6.094$ kcal mol^{-1}) than that of the wild-type p7B TMD. Therefore, a simultaneous and/or a higher modification of the putative topological determinants might be necessary to invert the p7B membrane orientation, suggesting strong stability of the MP in the ER membrane. Similar results have also been reported for *Carnation mottle virus* p9 MP using a heterologous system (51).

Finally, according to the observation that movement-competent p7B mutations do not affect p7B subcellular localization, both the $Y_{13}A$ and $Y_{28}A$ mutants were properly targeted to the ER, GA, and Pd, but unexpectedly, local spread of the corresponding mutant RNAs was significantly higher than that of wild-type RNA. The Y13 residue is located at the amino end of the TMD. After membrane insertion, it is most likely to be positioned at the membrane-cytoplasm interface. Interfacial aromatic residues, commonly found among membrane proteins, are important for the positioning and anchoring of the TMD in the lipid bilayer. In this scenario, the precise positioning of p7B relative to the membrane does not appear to be essential for its function; nonetheless, the lack of anchoring restrictions can favor lateral mobility of p7B between different ER subdomains (for example, ER export sites [ERES]), resulting in increased intracellular transport efficiency, which, consequently, may facilitate MNSV local infection progress. A similar effect can be produced when the snorkeling effect of Y28 is removed.

In summary, the results presented here demonstrate that the p7B Golgi apparatus-mediated traffic to Pd is essential for efficient MNSV cell-to-cell movement. Moreover, the multiple structural requirements of the MP appear to be involved in controlling Pd targeting. This probably reflects the multiple interactions that must occur between cellular factors and this small MP to guarantee functionality in the appropriate destination, the Pd. Similarly, multiple cytosolic and transmembrane determinants are also required for SCAMP1 trafficking via an ER/GA/*trans*-Golgi network/plasma membrane pathway (10). Therefore, the reduced size and simple topology of p7B make this a useful system to gain a better understanding not only of the trafficking mechanism of single transmembrane proteins, but of the interactions taking place between the viral protein and the cellular environment during the viral life cycle.

ACKNOWLEDGMENTS

Work in our laboratory has been supported by grant BIO08-03528 from the Spanish granting agency DGICYT and by grant ACOMP 2011-074 from the Generalitat Valenciana. J.A.N. and A.G. are recipients of a postdoctoral contract and a Ph.D. fellowship from the Spanish Ministerio de Ciencia e Innovación.

We thank M. C. Herranz for critical reading of the manuscript and V. V. Dolja (Oregon State University, Corvallis, OR) for kindly providing the STtmdChFP and MP(TMV)-mRFP binary vectors. PNRSV MP and mGFP5 binary vectors were a generous gift of J. A. Sánchez (IBMCP, Valencia, Spain) and C. Torres (IBMCP, Valencia, Spain), respectively. We thank L. Corachán and L. Latorre for their technical assistance.

REFERENCES

1. **Adams, M. J., and J. F. Antoniw.** 2005. Membrane proteins from plant viruses, p. 3–20. *In* W. B. Fischer (ed.),Viral membrane proteins: structure, function, and drug design. Kluwer Academic-Plenum Publishers, New York, NY.
2. **Aparicio, F., V. Pallás, and J. A. Sánchez-Navarro.** 2010. Implication of the C terminus of the Prunus necrotic ringspot virus movement protein in cell-to-cell transport and in its interaction with the coat protein. J. Gen. Virol. **91:**1865–1870.
3. **Aparicio, F., J. A. Sánchez-Navarro, and V. Pallás.** 2006. *In vitro* and *in vivo* mapping of the Prunus necrotic ringspot virus coat protein C-terminal dimerization domain by bimolecular fluorescence complementation. J. Gen. Virol. **87:**1745–1750.
4. **Barlowe, C.** 2003. Signals for COPII-dependent export from the ER: what's the ticket out? Trends Cell Biol. **13:**295–300.
5. **Bechinger, B.** 2001. Membrane insertion and orientation of polyalanine peptides: a 15N solid-state NMR spectroscopy investigation. Biophys. J. **81:**2251–2256.
6. **Brambillasca, S., et al.** 2005. Transmembrane topogenesis of a tail-anchored protein is modulated by membrane lipid composition. EMBO J. **24:**2533–2542.
7. **Brandizzi, F., et al.** 2002. The destination for single-pass membrane proteins is influenced markedly by the length of the hydrophobic domain. Plant Cell **14:**1077–1092.
8. **Brill, L. M., R. S. Nunn, T. W. Kahn, M. Yeager, and R. N. Beachy.** 2000. Recombinant Tobacco mosaic virus movement protein is an RNA-binding, alpha-helical membrane protein. Proc. Natl. Acad. Sci. U. S. A. **97:**7112–7117.
9. **Byers, J. T., R. M. Guzzo, M. Salih, and B. S. Tuana.** 2009. Hydrophobic profiles of the tail anchors in SLMAP dictate subcellular targeting. BMC Cell Biol. **10:**48.
10. **Cai, Y., et al.** 2011. Multiple cytosolic and transmembrane determinants are required for the trafficking of SCAMP1 via an ER-Golgi-TGN-PM pathway. Plant J. doi:10.1111/j.1365-313X.2010.04469.x.
11. **Chamberlain, A. K., Y. Lee, S. Kim, and J. U. Bowie.** 2004. Snorkeling preferences foster an amino acid composition bias in transmembrane helices. J. Mol. Biol. **339:**471–479.
12. **Ciczora, Y., N. Callens, K. Séron, Y. Rouillé, and J. Dubuisson.** 2010. Identification of a dominant endoplasmic reticulum-retention signal in yellow fever virus pre-membrane protein. J. Gen. Virol. **91:**404–414.
13. **Deber, C. M., and A. G. Therien.** 2002. Putting the β-breaks on membrane protein misfolding. Nat. Struct. Biol. **9:**318–319.
14. **Dowhan, W., and M. Bogdanov.** 2009. Lipid-dependent membrane protein topogenesis. Annu. Rev. Biochem. **78:**515–540.
15. **Dunlop, J., P. C. Jones, and M. E. Finbow.** 1995. Membrane insertion and assembly of ductin: a polytopic channel with dual orientation. EMBO J. **14:**3609–3616.
16. **Fujiki, M., S. Kawakami, R. W. Kim, and R. N. Beachy.** 2006. Domains of tobacco mosaic virus movement protein essential for its membrane association. J. Gen. Virol. **9:**2699–2707.
17. **Gavel, Y., and G. von Heijne.** 1992. The distribution of charged amino acids in mitochondrial inner-membrane proteins suggests different modes of membrane integration for nuclearly and mitochondrially encoded proteins. Eur. J. Biochem. **205:**1207–1215.
18. **Genovés, A., J. A. Navarro, and V. Pallás.** 2006. Functional analysis of the five Melon necrotic spot virus genome-encoded proteins. J. Gen. Virol. **87:**2371–2380.
19. **Genovés, A., J. A. Navarro, and V. Pallás.** 2009. A self-interacting carmovirus movement protein plays a role in binding of viral RNA during the cell-to-cell movement and shows an actin cytoskeleton dependent location in cell periphery. Virology **395:**133–142.
20. **Genovés, A., J. A. Navarro, and V. Pallás.** 2010. The intra- and intercellular movement of Melon necrotic spot virus (MNSV) depends on an active secretory pathway. Mol. Plant Microbe Interact. **23:**263–272.
21. **Goder, V., and M. Spiess.** 2003. Molecular mechanism of signal sequence orientation in the endoplasmic reticulum. EMBO J. **22:**3645–3653.
22. **Granseth, E., G. von Heijne, and A. Elofsson.** 2005. A study of the membrane-water interface region of membrane proteins. J. Mol. Biol. **346:**377–385.
23. **Guenoune-Gelbart, D., M. Elbaum, G. Sagi, A. Levy, and B. L. Epel.** 2008. *Tobacco mosaic virus* (TMV) replicase and movement protein function synergistically in facilitating TMV spread by lateral diffusion in the plasmodesmal desmotubule of *Nicotiana benthamiana*. Mol. Plant Microbe Interact. **21:**335–345.
24. **Harries, P. A., et al.** 2009. Differing requirements for actin and myosin by plant viruses for sustained intercellular movement. Proc. Natl. Acad. Sci. U. S. A. **106:**17594–17599.
25. **Hessa, T., et al.** 2005. Recognition of transmembrane helices by the endoplasmic reticulum translocon. Nature **433:**377–381.
26. **Hessa, T., S. H. White, and G. von Heijne.** 2005. Membrane insertion of a potassium channel voltage sensor. Science **307:**1427.

27. **Hessa, T., et al.** 2007. Molecular code for transmembrane-helix recognition by the Sec61 translocon. Nature **450:**1026–1030.
28. **Higy, M., T. Junne, and M. Spiess.** 2004. Topogenesis of membrane proteins at the endoplasmic reticulum. Biochemistry **43:**12716–12722.
29. **Huang, M., L. Jongejan, H. Zheng, L. Zhang, and J. F. Bol.** 2001. Intracellular localization and movement phenotypes of *Alfalfa mosaic virus* movement protein mutants. Mol. Plant Microbe Interact. **14:**1063–1074.
30. **Huang, M., and L. Zhang.** 1999. Association of the movement protein of *Alfalfa mosaic virus* with the endoplasmic reticulum and its trafficking in epidermal cells of onion bulb scales. Mol. Plant Microbe Interact. **12:**680–690.
31. **Kawakami, S., Y. Watanabe, and R. N. Beachy.** 2004. Tobacco mosaic virus infection spreads cell to cell as intact replication complexes. Proc. Natl. Acad. Sci. U. S. A. **101:**6291–6296.
32. **Knoester, M., et al.** 1998. Ethylene-insensitive tobacco lacks non-host resistance against soil-borne fungi. Proc. Natl. Acad. Sci. U. S. A. **95:**1933–1937.
33. **Laliberté, J. F., and H. Sanfaçon.** 2010. Cellular remodeling during plant virus infection. Annu. Rev. Phytopathol. **48:**69–91.
34. **Lerch-Bader, M., C. Lundin, H. Kim, I. Nilsson, and G. von Heijne.** 2008. Contribution of positively charged flanking residues to the insertion of transmembrane helices into the endoplasmic reticulum. Proc. Natl. Acad. Sci. U. S. A. **105:**4127–4132.
35. **Liang, J., L. Adamian, and R. Jackups, Jr.** 2005. The membrane-water interface region of membrane proteins: structural bias and the anti-snorkeling effect. Trends Biochem. Sci. **30:**355–357.
36. **Liu, L. P., and C. M. Deber.** 1999. Combining hydrophobicity and helicity: a novel approach to membrane protein structure prediction. Bioorg. Med. Chem. **7:**1–7.
37. **Lucas, W. J.** 2006. Plant viral movement proteins: agents for cell-to-cell trafficking of viral genomes. Virology **344:**169–184.
38. **Lundin, C., H. Kim, I. Nilsson, S. White, and G. von Heijne.** 2008. The molecular code for protein insertion in the ER membrane is similar for N_{in}-C_{out} and N_{out}-C_{in} transmembrane helices. Proc. Natl. Acad. Sci. U. S. A. **105:**15702–15707.
39. **Mandahar, C. L.** 2006. Multiplication of RNA plant virus. Springer-Verlag, Dordrecht, The Netherlands.
40. **Martínez-Gil, L., A. Saurí, M. Vilar, V. Pallás, and I. Mingarro.** 2007. Membrane insertion of the p7B movement protein of *Melon necrotic spot virus* (MNSV). Virology **367:**348–357.
41. **Martínez-Gil, L., et al.** 2009. Plant virus cell-to-cell movement is not dependent on the transmembrane disposition of its movement protein. J. Virol. **83:**5535–5543.
42. **Navarro, J. A., et al.** 2006. RNA-binding properties and membrane insertion of Melon necrotic spot virus (MNSV) double gene block movement proteins. Virology **356:**57–67.
43. **Nilsson, J., B. Persson, and G. von Heijne.** 2005. Comparative analysis of amino acid distributions in integral membrane proteins from 107 genomes. Proteins **60:**606–616.
44. **Peremyslov, V. V., Y. W. Pan, and V. V. Dolja.** 2004. Movement protein of a closterovirus is a type III integral transmembrane protein localized to the endoplasmic reticulum. J. Virol. **78:**3704–3709.
45. **Reichel, C., and R. N. Beachy.** 1998. Tobacco mosaic virus infection induces severe morphological changes of the endoplasmic reticulum. Proc. Natl. Acad. Sci. U. S. A. **19:**11169–11174.
46. **Ren, J., S. Lew, Z. Wang, and E. London.** 1997. Transmembrane orientation of hydrophobic α-helices is regulated both by the relationships of helix length to bilayer thickness and by cholesterol concentration. Biochemestry **36:**10213–10220.
47. **Riek, R. P., I. Rigoutsos, J. Novotny, and R. M. Graham.** 2001. Non-alpha-helical elements modulate polytopic membrane protein architecture. J. Mol. Biol. **306:**349–362.
48. **Sagi, G., A. Katz, D. Guenoune-Gelbart, and B. L. Epel.** 2005. Class 1 reversibly glycosylated polypeptides are plasmodesmal-associated proteins delivered to plasmodesmata via the Golgi apparatus. Plant Cell **17:**1788–1800.
49. **Sambade, A., and M. Heinlein.** 2009. Approaching the cellular mechanism that supports the intercellular spread of *Tobacco mosaic virus*. Plant Signal Behav. **4:**35–38.
50. **Saurí, A., P. J. McCormick, A. E. Johnson, and I. Mingarro.** 2007. Sec61alpha and TRAM are sequentially adjacent to a nascent viral membrane protein during its ER integration. J. Mol. Biol. **366:**366–374.
51. **Saurí, A., S. Tamborero, L. Martínez-Gil, A. E. Johnson, and I. Mingarro.** 2009. Viral membrane topology is dictated by multiple determinants in its sequence. J. Mol. Biol. **387:**113–128.
52. **Scholthof, H. B.** 2005. Plant virus transport: motions of functional equivalence. Trends Plant Sci. **10:**376–382.
53. **Schwartz, M., J. Chen, W.-M. Lee, M. Janda, and P. Ahlquist.** 2004. Alternate, virus-induced membrane rearrangements support positive-strand RNA virus genome replication. Proc. Natl. Acad. Sci. U. S. A. **101:**11263–11268.
54. **Szczesna-Skorupa, E., and B. Kemper.** 2000. Endoplasmic reticulum retention determinants in the transmembrane and linker domains of cytochrome P450 2C1. J. Biol. Chem. **275:**19409–19415.
55. **Taliansky, M., L. Torrance, and N. O. Kalinina.** 2008. Role of plant virus movement proteins. Methods Mol. Biol. **451:**33–54.
56. **Thomas, C., E. M. Bayer, C. Ritzenthaler, L. Fernandez-Calvino, and A. J. Maule.** 2008. Specific targeting of a plasmodesmal protein affecting cell-to-cell communication. PLoS Biol. **6:**1–11.
57. **Verchot-Lubicz, J., et al.** 2010. Varied movement strategies employed by triple gene block-encoding viruses. Mol. Plant Microbe Interact. **23:**1231–1247.
58. **von Heijne, G.** 1991. Proline kinks in transmembrane α-helices. J. Mol. Biol. **218:**499–503.
59. **von Heijne, G.** 2006. Membrane-protein topology. Nat. Rev. Mol. Cell Biol. **7:**909–918.
60. **von Heijne, G.** 2007. Formation of transmembrane helices *in vivo*—is hydrophobicity all that matters? J. Gen. Physiol. **129:**353–356.
61. **White, S. H., and G. von Heijne.** 2005. Transmembrane helices before, during and after insertion. Curr. Opin. Struct. Biol. **15:**378–386.
62. **Zamyatnin, A. A., Jr., et al.** 2006. Assessment of the integral membrane protein topology in living cells. Plant J. **46:**145–154.